

Diffusive Spreading Across Dynamic Mitochondrial Network Architectures

Keaton B. Holt,¹ Camryn Zurita,² Lizzy Teryoshin,¹ Samantha C. Lewis,^{2,3,4} and Elena F. Koslover^{1,*}

¹*Department of Physics, University of California, San Diego, San Diego, California 92093*

²*Department of Molecular and Cell Biology, University of California, Berkeley, Berkeley, California 94720*

³*Innovative Genomics Institute, Berkeley, California 94720*

⁴*Helen Wills Neuroscience Institute, Berkeley, California 94720*

(Dated: August 29, 2025)

Networks of physical units can vary from a stationary set of spatially-embedded links to a collection of mobile agents that undergo transient social interactions. In living cells, mitochondria form architectures that span across these regimes, transitioning between fragmented, partly connected, and highly fused structures depending on cell type and state. Diffusive transport of biomolecular components through these networks limits the heterogeneity of the mitochondrial population. Here we address the connection between dynamic network architecture and the rate of diffusive mixing through simulations and analytic models that incorporate fusion, fission, and rearrangement. We find that the material delivered from a source to the rest of the network depends on the network dimensionality and a balance of competing timescales for encounter, fusion, and diffusive dispersion. We extract morphological and dynamic parameters for mitochondrial networks in three human cell lines, demonstrating that different cells span across both the physical and social network regimes. Mixing in mitochondrial networks is shown to be limited by material transport through connected tubules for slowly-diffusing particles and by inter-mitochondrial encounter rates for rapidly diffusing ones. These results provide a quantitative basis for predicting the homogenization of proteins, lipids, ions, or genetic material through the mitochondrial population. The general principles identified in this work capture diffusive spreading through both social and physical networks, unifying a continuum of spatial network architectures.

INTRODUCTION

Diffusive transport through networks has been studied in a variety of contexts, including disease spread in epidemiology [1, 2], innovations in social networks [3], communication among insects [4, 5], diffusion of signals and nutrients in the brain extracellular space [6, 7], and oil recovery in porous rock [8]. These systems can be separated into two broad classes: one where the topology of network connections is stationary and limited to nearest neighbors, and another where network nodes are mobile and promiscuous, interacting with many different partners over time.

Physical networks form an important category of stationary, spatially-constrained network structures [9]. In such networks, edges represent objects subject to physical limitations (space-filling, steric repulsion, etc.) [10, 11] connecting degree-1 tips and degree-3 junctions, with higher degree nodes exceedingly rare [12, 13]. Examples include fungal mycelia [14], neuronal synaptic networks [15], and interconnected pores in rocks [16]. Transport behaviors on stationary networks can be described by the graph Laplacian, whose eigenvalues govern the spreading timescales [17–19]. In some percolation problems, physical networks become dynamic as edges are allowed to flicker between an active and inactive state [20, 21].

A distinct set of approaches considers signal transmission in ‘social’ networks of transiently-interacting mobile

units. In such networks, the mixing behavior is defined by distributions of contact durations and inter-contact times [4, 22], which may be constrained by spatial embedding [1, 2]. Notably, many previously studied social network systems focus on the spreading of a non-diluting signal (infection, information, etc.) [2–4], in contrast to dispersion of mass-conserving physical material [21, 23, 24].

Despite the distinct modeling approaches employed, physical and social networks lie on a continuum of temporal network structures [22] with varying timescales of topological rearrangement. The intracellular environment exemplifies this spectrum. The endoplasmic reticulum forms a well-connected physical lattice of membrane-bound tubules that enables diffusive transport of proteins [24] and ions [25] across the entire cell. At the opposite extreme, the population of endocytic vesicles constitutes a social network of discrete transiently-interacting compartments [26, 27].

Mitochondria form another intracellular network with striking structural variability. Mitochondrial network architectures vary across cell types [28–31], and transition between fragmented and hyperfused states in response to disease [32–37], metabolic conditions [38–40], calcium signalling and apoptosis [41, 42], and cell cycle progression [43, 44]. These structural changes are thought to support important functions such as genetic complementation [45, 46], dilution of harmful reactive oxygen species (ROS) [47], power cabling [48, 49], quality control [50–53], and modulation of mitochondrial heterogeneity across the population [54, 55]. These cellular functions rely on the connectivity-dependent diffusive spread of proteins, lipids, and/or ions through the under-

* ekoslover@ucsd.edu

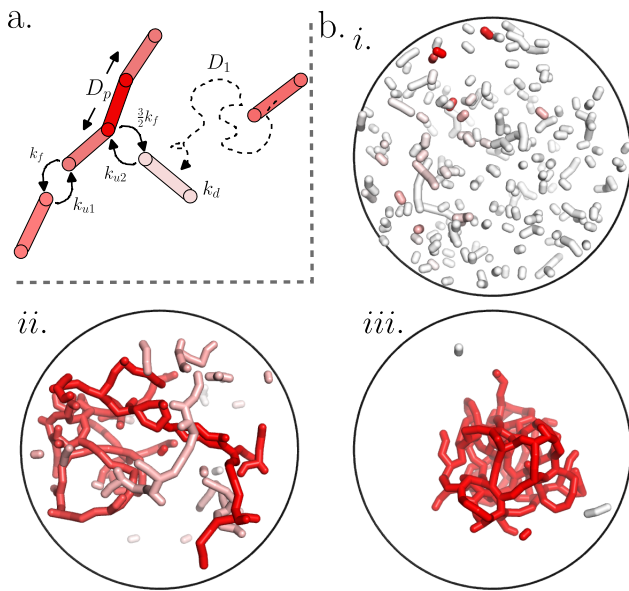


FIG. 1. Dynamic network simulation framework. (a) A network is formed by interacting units which diffuse through 3D space with diffusivity D_1 . Nearby units can undergo tip-tip and tip-side fusion with rates k_{u1}, k_{u2} while connected nodes undergo fission at rate $k_f, \frac{3}{2}k_f$, respectively. Material spreads along connected units with diffusivity D_p and decays over time with rate k_d . Red indicates the concentration of material in a given unit. (b) Snapshots of spreading on simulated networks at steady state. (i) Fragmented network, ($k_{u1}/k_f = 30$) (ii) Network near percolation transition, with kinetic parameters appropriate to mammalian mitochondrial networks [57] ($k_{u1}/k_f = 1000$). (iii) Hyperfused network ($k_{u1}/k_f = 3000$). The ratio of tip-tip and tip-side fusion is set to $k_{u1} = 3k_{u2}$, and particle diffusivity is $D_p = 4800$ throughout.

lying mitochondrial network [21, 56].

To elucidate how mitochondrial structure and dynamics govern the mixing of effectively diffusive particles, we introduce a quantitative framework for transport on spatially-embedded dynamic networks. We show that network connectivity governs spreading behavior by modulating several competing timescales: the cluster filling rate, encounter rate, and fusion rate, as well as the decay rate of the spreading material. In particular, we demonstrate a transition from rapid but low-dimensional spread in well-connected networks to slower three-dimensional spreading through an interacting population. Due to the different dimensionalities involved, particles with distinct diffusivities and networks with distinct structures can exhibit qualitatively different scaling behavior for dispersion from a source. We use the model to predict spreading rates for mitochondrial networks in three different human cell types, demonstrating the structural diversity and different regimes of relevance for these networks.

MODEL DESCRIPTION

We seek to quantify the rate of material dispersion through dynamic spatial networks ranging from the social to the physical regime. These limiting architectures, as well as a continuum of intermediate network connectivities, are encompassed by a simulation framework [57], illustrated in Fig. 1, consisting of N_0 interacting spherocylindrical units of length ℓ_0 , which move diffusively through a bounded spherical domain of radius R with unit diffusivity D_1 . Upon close encounters, pairs of units may fuse into larger clusters with rate constants k_{u1} (for tip-tip fusions) or k_{u2} (for tip-side fusions). Fission breaks connections at the nodes, with fission rate proportional to the number of attached edges (k_f at degree-2 nodes and $1.5k_f$ at degree-3 nodes), in keeping with prior models [13]. At steady state, the system exhibits a characteristic mean cluster size $\langle n \rangle$ set by the balance of fusion and fission, and an associated cluster diffusivity D_n . Details of this structural model and parameterization are described in Ref. [57]; here we focus on the spreading of material throughout the resulting dynamic networks.

We select at random a single unit, which serves as a particle source with fixed constant concentration $h_0 = 1/\ell_0$. Such a fixed source could represent, for instance, an import site for nucleus-encoded proteins [58], a site of regulated translation at a mitochondrial RNA granule or nucleoid [59], or a location of calcium entry at a contact with the endoplasmic reticulum [60]. The concentration field is propagated between connected units on the network with effective diffusivity D_p , using a finite volume approach [61] discretized at the level of individual units. Concentrations decay with a constant rate k_d (representing removal from the network). The decay rate serves to set a relevant timescale, with the resulting calculations closely related to the question of how much material spreads from the source over a certain time. We quantify dispersion by computing the total amount of material (S) in the network at steady-state, excluding the source unit. Example steady-state snapshots are shown in Fig. 1b and Supplemental Video 1.

Given the complex internal structure of mitochondria and the variety of functionally relevant biomolecules within them, particle diffusivities can vary broadly. For example, proteins in the inner mitochondrial membrane can be embedded in the extensive folds of cristae [62]. The cristae also serve as diffusive barriers to hinder transport of solutes in the matrix [63] and intermembrane space [64]. Our simplified modeling approach coarse-grains these complications into a single effective diffusivity D_p representing the motion of a particle along the mitochondrial tubule axis. Reported effective diffusivities vary over orders of magnitude, from $\sim 0.004\mu\text{m}^2/\text{s}$ for ATP synthase components [65], to $\sim 20\mu\text{m}^2/\text{s}$ for mitochondrial matrix proteins [66], with diffusivity of ions presumed even higher [67]. We consider a range of diffusivities $D_p = 0.4 - 40\mu\text{m}^2/\text{s}$ in our simulations. The diffusivity of individual mitochondria is estimated to be

much slower, at $D_1 \approx 0.25 \mu\text{m}^2/\text{min}$ [28, 68].

The results below are reported in dimensionless units, relative to the length scale $2\ell_0$ and the timescale $1/k_f$. A reasonable estimate sets the mitochondrial unit length to $\ell_0 = 0.5 \mu\text{m}$ and the fission timescale to $1/k_f \approx 2 \text{ min}$ [57], consistent with experimental measurements of overall fission rate [28, 69]. The corresponding dimensionless diffusivities are $D_p = 48 - 4800$ for the material, and $D_1 = 0.5$ for individual mitochondria.

RESULTS

Spreading on the network is governed by the interplay of several key timescales: the decay time $\tau_d = 1/k_d$, the cluster filling time τ_c for particles to diffusively explore a typical-sized connected component (cluster), and the waiting time between interactions τ_{int} (the time to encounter and fuse with a new cluster). The fission time $\tau_f = 1/k_f$ sets the typical duration of transient interactions between distinct clusters. The material exhibits different dynamics depending on the comparative values of these four timescales. We begin by considering several limiting regimes where different timescales dominate.

Highly connected regime: spreading through stationary networks

In the limit where τ_d is the shortest timescale, material spreads primarily within a single connected component. This regime is relevant for highly fused networks with large cluster sizes. Such networks tend to be relatively static in their topology, with any fissions that occur rapidly followed by re-fusion with the same neighboring unit [57]. Recent evidence of colocalizing mitochondrial fusion and fission machinery at ER-mitochondria contact sites also points towards increased likelihood of re-fusion following a fission event [70].

For static networks, the steady-state distribution of material can be found by solving the diffusion equation on each one-dimensional edge, while matching boundary conditions at each node (details in SI Appendix). This method provides an exact solution for each individual network structure. However, to gain insight on the relevant scaling regimes, we turn to a mean-field continuum approach.

Depending on the relative rates of tip-tip versus tip-side fusion, network architectures can range from near-linear snake-like structures to highly branched compact morphologies, with the latter allowing for more rapid spreading of material through the network (Fig. 2). These structural features can be described by an effective fractal dimension d , which sets the scaling relationship between the number of units and the network ‘size’ in terms of graph distance. Specifically, we count the number of nodes within a given graph distance from a starting node, averaged over all possible starting nodes [71]. The

power-law scaling exponent of this curve defines the dimension d (Fig. 2i, inset) and therefore the cluster filling timescale, $\tau_c = (\langle n \rangle^{1/d} \ell_0)^2 / D_p$. Although the simulated networks are embedded in a three-dimensional space, the limited junction degree gives rise to networks that are of lower dimension ($1 \leq d \leq 2$). This feature has been previously observed in a variety of physical networks, from plant roots to ant tunnels, composed of tube-like objects connected at junctions [12].

We first consider the limit where the diffusive length-scale $\lambda_p = \sqrt{D_p/k_d}$ is smaller or comparable to the length of linear segments between junctions. In the case of a completely linear snake-like network, the steady-state material content S_1 is given by the solution of the one-dimensional (1D) diffusion equation, $S_1 = \frac{n_b \lambda_p}{\ell_0} \tanh\left(\frac{\ell_0 \langle n \rangle / n_b}{\lambda_p}\right)$ with $n_b = 2$. When there are additional branches adjacent to the source ($d > 1$), more material is able to enter the network. We thus define n_b as the average number of edges directly connected to the source unit, and approximate the entire network cluster as a set of n_b linear spokes, each of length $\ell_0 \langle n \rangle / n_b$, connected to a central source (Fig. 2iv). S_1 then gives an estimate of the total material spreading over a short diffusive lengthscale λ_p (Fig. 2, dashed-circle curves).

For the regime where material spreads over a more extensive network structure (λ_p much greater than segment length), we consider diffusion through a d -dimensional medium. Here we approximate the spreading as spherically symmetric, with a d -sphere of radius a_n (enclosing the source edge) maintained at fixed concentration, and a reflecting d -sphere of radius R_n representing the outer boundary of the cluster. We set R_n such that the average distance between two points in the d -dimensional domain is equal to the average graph distance between network nodes (details in SI Appendix). Assuming that the $\langle n \rangle$ network units are uniformly distributed within the continuum sphere, the radius a_n is set proportionately to allow for 1 source unit within the inner sphere: $1/a_n^d = (\langle n \rangle - 1)/(R_n^d - a_n^d)$.

We can write down the diffusion equation in d -space, $(\frac{1}{d} D_p) \frac{1}{r^{d-1}} \frac{\partial}{\partial r} \left(r^{d-1} \frac{\partial c(r)}{\partial r} \right) - k_d c(r) = 0$, where the effective particle diffusivity is scaled by the dimension d . This scaling is applied because, when diffusing along an edge, the particle only moves in one dimension at each instance in time rather than simultaneously in all d dimensions. The d -space diffusion equation has solutions in terms of modified Bessel functions $I_\nu(x), K_\nu(x)$ [72], where $\nu = 1 - d/2$ and $x = r\sqrt{d}/\lambda_p$. Taking a fixed concentration boundary at $x_1 = a_n\sqrt{d}/\lambda_p$ and a reflecting boundary at $x_2 = R_n\sqrt{d}/\lambda_p$ we find the total material delivered (details in SI Appendix):

$$S_d = \frac{d}{x_1} \frac{[-I_{\nu-1}(x_1)K_{\nu-1}(x_2) + I_{\nu-1}(x_2)K_{\nu-1}(x_1)]}{[I_\nu(x_1)K_{\nu-1}(x_2) + I_{\nu-1}(x_2)K_\nu(x_1)]} \quad (1)$$

Fig. 2 shows the correspondence between diffusion through a fractal continuum (dashed-square curves) and

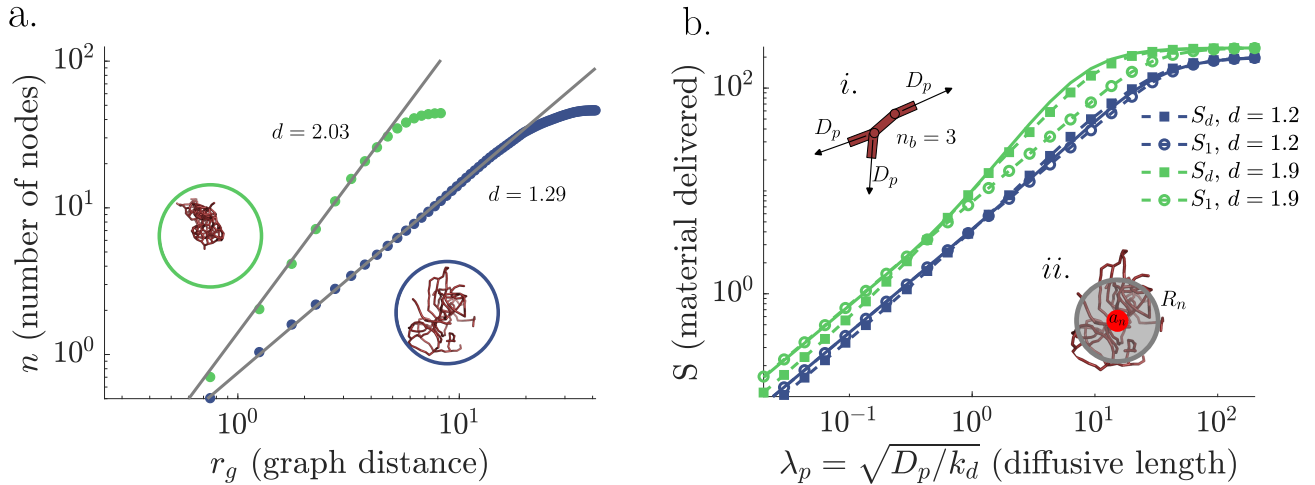


FIG. 2. Material spreading on static networks of different dimension d . Two different sets of networks are considered: near-linear structures (blue) with $k_{u2} = 0.01k_{u1}$ and highly-branched structures (green) with $k_{u2} = 10k_{u1}$. The simulations are run to steady state, and the network structures are then frozen. (a) Calculation of the network dimension for a single instance of each network type (shown in inset). The number of nodes within a given graph distance is plotted against the graph distance on log-log axes, with the slope giving the dimension, d . Averaging over 21 snapshots from 3 independent simulations yields effective dimensionalities $d = 1.2$, $d = 1.9$, respectively. (b) Total material delivered from a source unit on the static networks is plotted as a function of the diffusive lengthscale, $\lambda_p = \sqrt{D_p/k_d}$. Solid curves show exact solution (details in SI Appendix), averaged over replicate snapshots. Dashed-circle curves show approximation with the linear motif (inset i), applicable at short λ_p . Dashed-square curves show continuum solution on a fractal domain (inset ii), matching well at long λ_p .

the exact solution (solid curves) for networks with different connectivities. The linear motif solution S_1 is a good estimate for small diffusive lengths, while the continuum solution S_d is a better approximation for large λ_p . When the diffusive lengthscale is large enough ($\lambda_p > R_n$), the entire connected component saturates. Overall, material delivery is boosted by increased network branching [21], which increases both the network dimension and the network density (lower R_n for the same number of network units).

Fragmented network regime: spreading through transient interactions

We next consider the regime of highly fragmented ‘social’ networks, where clusters are sufficiently small (and particle diffusivity sufficiently fast) that concentrations are fully equilibrated within each cluster: $\tau_c \ll \{\tau_d, \tau_{\text{int}}\}$. In this limit, we can approximate the network as a system of $N = N_0/\langle n \rangle$ identical spherical units with effective radius a , each representing a cluster of uniform concentration. These effective units are capable of undergoing transient fusions whenever they are within contact radius b , with local rate constant k_u . Each fusion equilibrates the particle concentration in the two units involved, and is instantaneously followed by fission so that no larger structures are formed.

Results from an explicit simulation of this simplified model are shown in Fig. 3 (dots). A mean-field analytic approximation can be found by fixing the source unit in

the center of a domain, assigning a diffusivity of $D = 2D_n$ to the remaining units and solving for the spatial concentration field $h(r, t)$, which defines the mean concentration per network unit located at distance r from the origin. The average of this field within the narrow contact zone is defined as $h_c(t)$. The time evolution of the concentration fields can be expressed as follows (details in SI Appendix):

$$\frac{dh(r, t)}{dt} = D\nabla^2 h(r, t) - k_d h(r, t), \quad \text{for } b < r < R \quad (2a)$$

$$\frac{dh_c(t)}{dt} = k_u [h_0 \ell_0 - h_c(t)] - \frac{I}{\rho v_c} - k_d h_c(t), \quad (2b)$$

where $k_u [h_0 \ell_0 - h_c(t)]$ represents the injection of new material into the system via fusion with the source, $I = -4\pi b^2 \rho D \left. \frac{dh(r, t)}{dr} \right|_b$ is the current of material leaving the contact zone, $\rho = (N_0 - \langle n \rangle)/V$ is the density of network units, $V = 4/3\pi(R^3 - a^3)$ is the domain volume, and $v_c = 4/3\pi(b^3 - a^3)$ is the contact zone volume. Interactions between non-source units do not alter the mean-field concentrations, and the overall material in the system can only increase upon encounters with the source.

We compute the steady-state solution of Eq. 2 and integrate $h(r)$ over space to find the total amount of material (S) in the system, excluding the source unit (details in

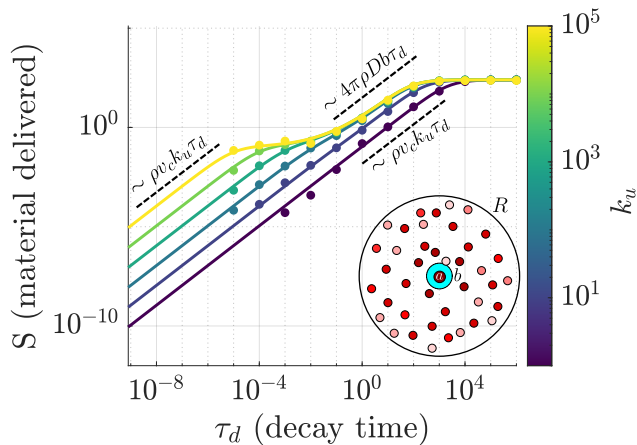


FIG. 3. Material delivered from a source unit in a system of fragmented clusters. Solid lines show mean-field solutions (see Eq. 3) with unit cluster size $\langle n \rangle = 1$, for different fusion rates k_u . Colored dots show explicit simulation results for a simplified system of interacting spheres with uniform size (inset). Dashed black lines show the limiting behavior for fusion-limited and encounter-limited regimes.

SI Appendix):

$$S = (\langle n \rangle - 1) + \rho h_c (v_c + z), \quad (3a)$$

$$h_c = \frac{1}{1 + k_d/k_u + k_d z / (k_u v_c)}, \quad (3b)$$

$$\frac{z}{4\pi b \lambda} = \frac{(\lambda - b)(R + \lambda) + (\lambda + b)(R - \lambda)e^{2(R-b)/\lambda}}{(R + \lambda) + (R - \lambda)e^{2(R-b)/\lambda}}, \quad (3c)$$

where $\lambda = \sqrt{D/k_d}$ is the diffusive lengthscale for spreading through the population of clusters. Here, the first term in S represents material in the cluster containing the source unit, the term $\rho h_c v_c$ is the total material within the contact layer (defined by a balance of fusion, decay, and diffusive escape), and z describes the additional volume over which the material has spread beyond the contact zone.

The total material in the system exhibits distinct scaling behaviors (Fig. 3, dashed) depending on the relative timescales for decay, encounter ($\tau_{\text{enc}} = (4\pi D b \rho)^{-1}$), and fusion ($\tau_u = (k_u \rho v_c)^{-1}$). In keeping with standard results for diffusion to a partially reactive target [73], the overall interaction time is given by the sum of waiting times for the two-step process: $\tau_{\text{int}} = \tau_{\text{enc}} + \tau_u$. In the limit of fast decay ($\tau_d \ll \tau_{\text{int}}$), the steady-state material in a social network of unit-size clusters approaches $S \rightarrow \rho v_c h_c = \rho v_c k_u / k_d$. In this limit, the total amount delivered is set by the number of units in the contact zone (ρv_c) and how often they fuse with the source during the decay time (k_u / k_d), with no spatial spread.

Another limit arises when diffusion of clusters is fast relative to both decay and fusion ($\tau_{\text{enc}} \ll \tau_d, \tau_u$). This yields the same scaling for the total network content $S \rightarrow \rho v_c k_u / k_d$, with $h_c \rightarrow k_u v_c / 4\pi D b$. The amount of

material in the contact layer (h_c) is set by a balance between injection through fusion (at rate $k_u \rho v_c$) and escape through the diffusive arrival of fresh units that dilute the local concentration ($4\pi D b \rho$). The additional volume $z \rightarrow 4\pi D b / k_d$ over which the material spreads depends on the balance between diffusive encounters and decay. Overall, the total amount of material in the network is fusion-limited as the rapid encounters quickly homogenize the individual units within the diffusive range of the source.

In a third limit, fusion of clusters is fast and decay is slow relative to the timescale of diffusive encounter. ($\tau_u \ll \tau_{\text{enc}} \ll \tau_d$). For this regime, the total material content is given by $S \rightarrow \rho z h_c \rightarrow 4\pi D b \rho / k_d$. This is an encounter-limited regime, where clusters arriving at the contact region fuse with the source nearly instantaneously ($h_c \approx h_0 \ell_0 = 1$), and spreading is determined by the balance of arrival and decay rates.

Fig. 3 shows the full solution of the mean-field model (Eq. 3) for spreading on a fragmented network, with variable fusion rate k_u and a unit cluster size $\langle n \rangle = 1$. The analytic calculations accurately reproduce simulations with diffusive spheres that exchange material via transient fusion (dots in Fig. 3, details in SI Appendix).

Dynamic networks with large interacting clusters

The model for spreading through a social network of interacting fragments can be expanded to approximate a regime with larger clusters. We use simulations of dynamic networks with different structures [57] to extract the effective parameters (mean cluster size $\langle n \rangle$, effective unit diffusivity D_n , steric radius a_n , contact volume v_c , and effective local fusion rate k_u) for the simplified social network model (details in SI Appendix).

When individual clusters are homogeneously filled upon each interaction ($\tau_c < \{\tau_d, \tau_{\text{int}}, \tau_f\}$), the solution in Eq. 3 can be used directly with the appropriate values of the parameters a, v_c, k_u . However, for slowly diffusing particles or very large clusters ($\tau_c > \tau_d$), the source cluster may be only partly full of material. The average concentration in the source cluster, $h_0^{(d)}$, is then determined by the static network solution (Eq. 1) within the cluster: $\ell_0 h_0^{(d)} = (S_d(\sqrt{D_p/k_d}) + 1)/\langle n \rangle$. When another cluster fuses with the source cluster, fission may terminate the encounter before filling is complete ($\tau_f < \tau_c$). The amount transferred should then be scaled by the fraction of the new cluster that is filled prior to fission: $f = (S_d(\sqrt{D_p/k_f}) + 1)/\langle n \rangle$. These two corrections modify the dynamic equation for the concentration in the contact zone (Eq. 2b) and its solution (Eq. 3a,b) as fol-

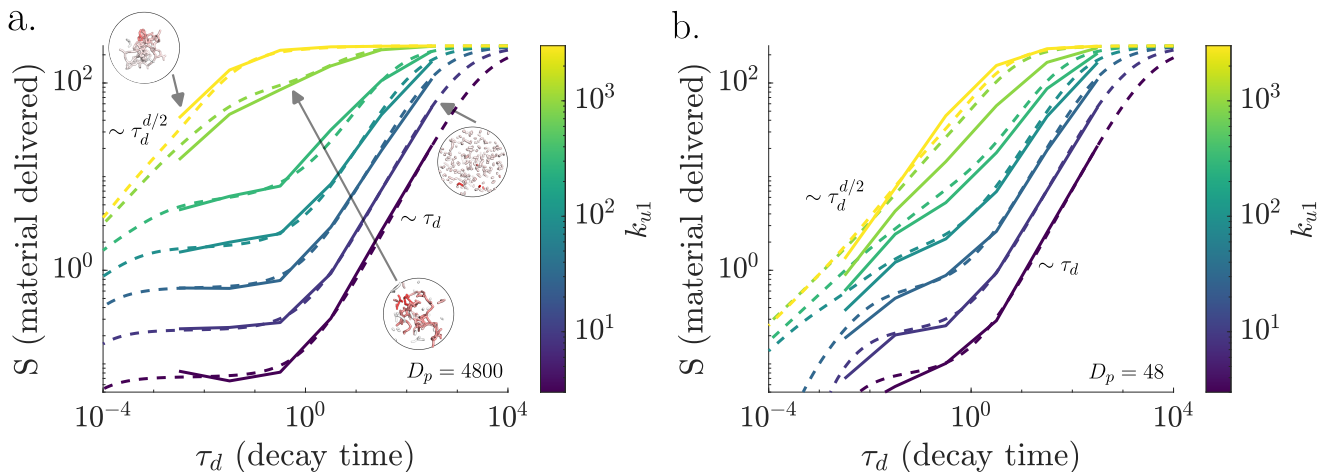


FIG. 4. Spreading on simulated networks exhibits a transition between the static network and social network regime. The total material is plotted as a function of the decay time for different fusion rate constants k_{u1} (solid lines). The analytic approximation (Eq. 4, dashed curves) encompasses both the fractal continuum limit (for large clusters or fast decay) and the social network limit (for small clusters and slow decay). Plateaus at intermediate decay times correspond to filling of an individual cluster before interactions can occur. Insets show example simulation snapshots for the parameters indicated by the gray arrows. Parameters $N_0 = 250, \ell_0 = 0.5, R = 5, k_{u2} = \frac{1}{3}k_{u1}, k_f = 1$ are used in both (a) and (b), with the particle diffusivity reduced from $D_p = 4800$ in (a) to $D_p = 48$ in (b).

lows:

$$\frac{dh_c(t)}{dt} = k_u \left[\ell_0 h_0^{(d)} - h_c(t) \right] f - \frac{I}{\rho v_c} - k_d h_c(t), \quad (4a)$$

$$S = S_d \left(\sqrt{D_p/k_d} \right) + \rho h_c(v_c + z), \quad (4b)$$

$$h_c = \frac{\ell_0 h_0^{(d)}}{1 + k_d/(f k_u) + k_d z/(f k_u v_c)}, \quad (4c)$$

where the first term in the updated S accounts for material in the source cluster and the second term represents material in the rest of the network. When clusters are large and interactions are infrequent, the above solution reduces to the static network limit of Eq. 1. When the clusters are small, the source cluster is fully filled ($h_0^{(d)} \rightarrow h_0$) and so is each cluster that interacts with it ($f \rightarrow 1$). The general solution then approaches the fragmented social network limit of Eq. 3.

In Fig. 4, we show the spreading of material through simulated networks with increasing connectivity, spanning across the different regimes. In the limit of rapid decay (small τ_d), material spreads within a single cluster of dimension d , with the amount delivered scaling as $S \sim \tau_d^{d/2}$. When particle diffusivity is fast and clusters are small, the source cluster fills faster than interactions can occur and the amount of material plateaus at the size of a single cluster, in the regime of $\tau_c < \tau_d < \tau_{\text{int}}$. For longer decay times, interaction between distinct clusters dominates the spread, and the total material scales linearly as $S \sim \tau_d$. When particle diffusion is slow (Fig. 4b), the cluster containing the source unit is able to offload material through interactions even before it is fully filled ($\tau_{\text{int}} < \tau_c$), and the plateau region narrows or disappears.

The simplified analytic model (Eq. 4) approximately matches simulations over a broad range of network connectivities and timescales (Fig. 4). However, some discrepancy occurs for networks that are close to the percolation transition (light green curve), particularly when the particle diffusivity is low. In this case, the approximation systematically overestimates material spreading through the network. This may be the result of transient fissions within a single cluster (which could temporarily hinder material spreading [21]), or steric inaccessibility of nodes buried within a cluster, neither of which are accounted for in our analytic models. Additionally, the percolation transition corresponds to a broad variability in cluster sizes [13], resulting in the source unit occasionally being trapped in very small clusters that limit material delivery.

The quantitative description of steady-state network filling (Eq. 4) can be generalized to other measures of material spread on a dynamic network. In particular, the decay time τ_d sets the timescale over which the spreading is assessed. The total amount of material delivered into the network over time is also well-approximated by the physical and social network models presented here (see Supplemental Fig. S1 in SI Appendix).

Spreading rates on mammalian mitochondrial networks

To illustrate the utility of our model in providing directly testable predictions for mitochondrial mixing, we analyze time-resolved images of fluorescently tagged mitochondria in three human cell lines: SH-SY5Y, IMR90,

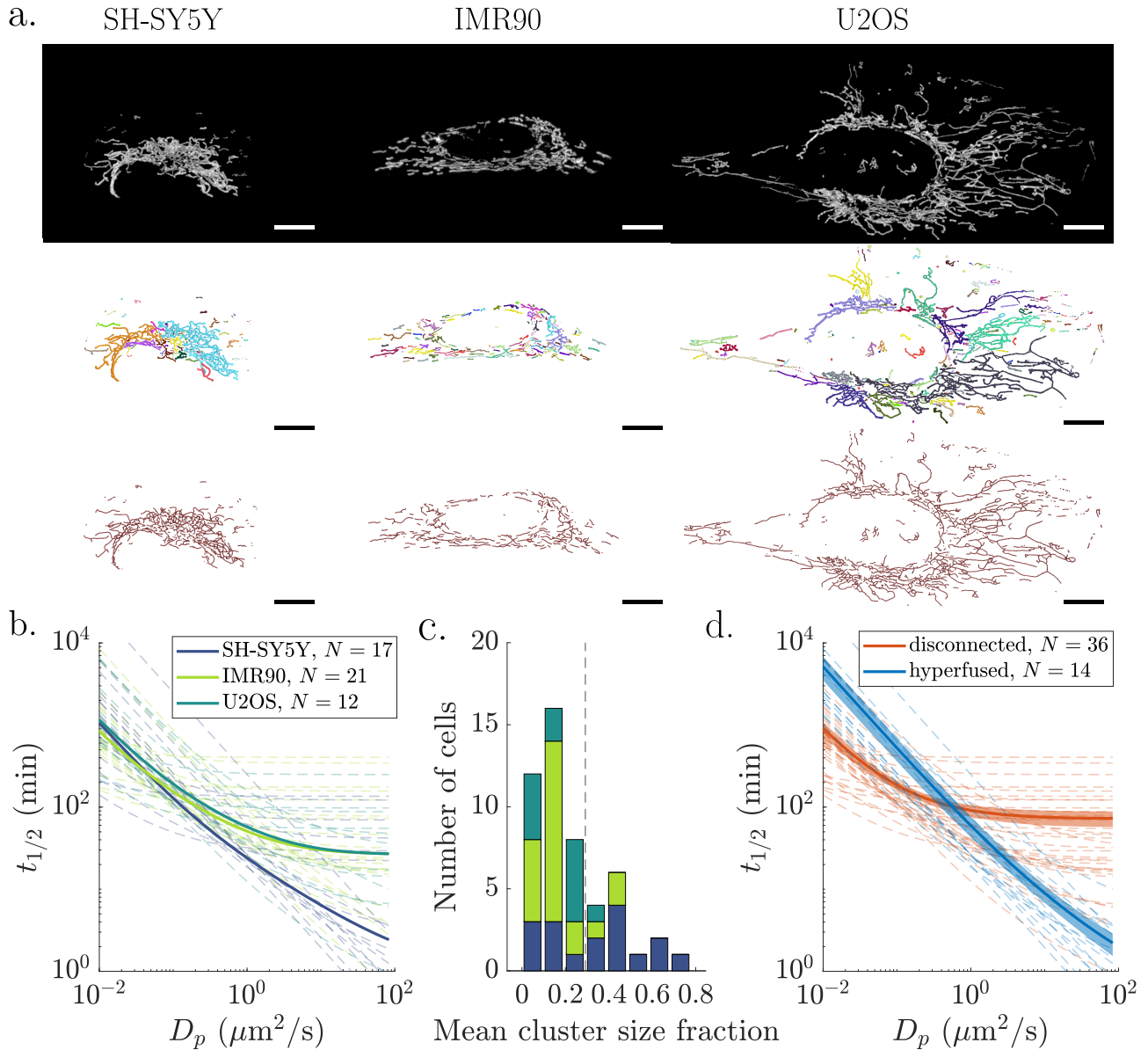


FIG. 5. Extracted structures of mammalian mitochondrial networks exemplify both the static network and social network regimes. (a) Representative raw, segmented, and skeletonized images (top to bottom) for mitochondria from SH-SY5Y (human neuroblastoma), IMR90 (human fibroblast), and U2OS (human osteosarcoma) cells. Segmented images show each connected cluster with a different color. Scale bar: $10\mu\text{m}$. (b) Time to fill half of the mitochondrial network with material supplied from a fixed source, as predicted by the analytic model, is plotted as a function of the material diffusivity for each cell type. Solid curves correspond to a ‘prototypical cell’, where parameters are averaged within each cell type before plugging into the analytic model. Dashed lines indicate results for individual cells. (c) The distribution of cells by mean cluster size fraction (mean cluster length divided by total mitochondrial network length). The dashed vertical line indicates the threshold (0.29) to classify networks as disconnected or hyperfused, as determined by k-means clustering with $k=2$. (d) Network filling half-times as in (b), with cells grouped by the mitochondrial network class (disconnected or hyperfused). Solid curves are obtained by averaging half-times across individual cells within each class with shaded regions indicating the standard error of the mean. Individual cell results are shown as dashed lines.

and U2OS. Specifically, we segment, skeletonize, and track the mitochondria of each cell in our data set (Figure 5a and Supplemental Video 2), extracting structural metrics (degree distribution, cluster size, fractal dimension) and dynamic parameters (fission rate and mito-

chondrial diffusivity). These values (provided in Supplemental Material) are used to parameterize our analytic model, which provides a quantitative estimate of mitochondrial material spreading. We estimate the time required for material to fill half the network ($t_{1/2}$) as the

value of τ_d corresponding to S reaching half its maximal value. This metric provides a prediction for how quickly particles of different types should spread through most of the mitochondrial network.

Figure 5b shows our predictions of spreading time on prototypical ‘average cells’, with individual parameters averaged across all the cells of that type. The spreading time is plotted as a function of the material diffusivity, D_p , in real units. For typical mitochondrial matrix proteins with $D_p = 20\mu\text{m}^2/\text{s}$ [66], we expect a spreading time of ~ 4 min for SH-SY5Y, and ~ 0.5 hr for IMR90 and U2OS cells. Notably, the different cell types exhibit distinct behaviors. For IMR90 and U2OS cells, the spreading time asymptotes for particle diffusivities above roughly $1\mu\text{m}^2/\text{s}$. By contrast, in the typical SH-SY5Y cell, spreading times continue to decrease with higher material diffusivity. These results arise primarily from differences in the network architecture: SH-SY5Y mitochondria tend to be hyperfused, while IMR90 and U2OS exhibit more disconnected networks, so that dispersion becomes limited by interactions between distinct mitochondrial clusters rather than diffusion within connected mitochondria. Overall, our results indicate that cultured human cell lines can vary substantially in their mitochondrial architecture and mixing dynamics.

It should be noted, however, that there is extensive variation in the mitochondrial structure and associated network parameters between individual cells of the same type (dashed lines in Fig. 5b). To further explore the dependence of spreading rates on network connectivity, we reclassified all cells in our data set as ‘disconnected’ or ‘hyperfused’ based on the mean cluster size as a fraction of the total mitochondrial population. Figure 5c shows the distribution of cells by mean cluster size fraction and the classification threshold obtained via a k-means clustering algorithm. All cells with mean cluster size fraction below the threshold were classified as disconnected, with the remainder considered hyperfused. Figure 5d demonstrates the difference in spreading behavior for these two cell classes, with hyperfused cells exhibiting strong dependence on material diffusivity across the entire relevant range. Spreading on disconnected networks plateaus for particles with diffusivities above $D_p \approx 1\mu\text{m}^2/\text{s}$. We note that for slowly diffusing material, disconnected networks can actually increase the spreading rate. This is due to the mobility of mitochondrial clusters, which allows each unit to interact with more neighbors than they could contact in the static low-dimensional hyperfused networks ($1 \leq d \lesssim 2$).

The mitochondrial networks for different cell types exhibit multiple morphological differences. In particular, the total network size in U2OS cells is substantially larger than in the other two cell types (Fig. 5a; see Supplemental Material). However, because the mean cluster size fraction is similar in both IMR90 and U2OS cells, the predicted filling half-time is similar as well. For systems that fall into the disconnected social network regime, it is the relative size of the individual mitochondrial clus-

ters compared to the full network that determines filling times.

The distinction in predicted spreading rates between different cell types can be attributed to their different propensities for mitochondrial connectivity. Many (though not all) SH-SY5Y cells exhibit hyperfused networks, while IMR90 and U2OS cells fall primarily in the disconnected category. SH-SY5Y cells thus serve as examples of the stationary physical network regime, where spreading is limited by material transport along a fractal-dimensional continuum. The other two cell types have mitochondria that behave akin to a social network, with interactions between clusters limiting the spread of rapidly diffusing particles. Notably, for both IMR90 and U2OS mitochondrial networks, the spreading at high D_p is limited by mitochondrial mobility rather than the timescale of local fusion or fission (see Supplemental Appendix). We note that the balance of fusion to fission rates, which sets network connectivity, plays an important role in dictating material spread. However, our analysis indicates that the interaction rate is limited by mitochondria moving through space to encounter new fusion partners rather than by the waiting time for fusion between two nearby mitochondria ($\tau_{\text{enc}} \gg \tau_u$). Thus, the model predicts that proportional increases in fusion and fission rates should have little effect on mitochondrial mixing.

DISCUSSION

In this work, we develop a mathematical framework for mixing of diffusive material in dynamic networks and apply it to mitochondrial networks in cultured human cells. We examine two limiting regimes: one of static, well-connected physical networks and one of socially interacting homogeneous clusters. In physical networks, spreading rates increase with material diffusivity and network dimensionality. In three-dimensional social networks, material accumulates linearly in time and is limited either by the fusion rate between nearby clusters or the mobility of those clusters.

The models presented here are based on measurable structural and dynamic features. The static model requires network dimensionality, cluster size, and particle diffusivity, while the social model additionally needs the fusion rate and cluster mobility as inputs. Modern imaging techniques allow quantification of mitochondrial network structure and dynamics in a variety of cellular systems [13, 28, 32, 74, 75]. Our results connect these morphological measurements to the dynamics of material spreading through the mitochondrial population.

We show example calculations for three human cell types, demonstrating the distinct parameter regimes accessed by their mitochondrial networks. For the set of cells considered here, many SH-SY5Y cells fall in the well-connected regime, while the majority of IMR90 and U2OS cells exhibit disconnected social mitochondrial net-

works, whose mixing is limited by mitochondrial mobility and encounter. It should be noted, however, that the mitochondrial structure varies substantially among individual cells of a given type, and is also expected to change as a function of metabolic conditions [38] and genetic perturbations [37, 75]. The predictions made by this model could be tested in future work by quantifying the dispersion of locally photoconverted proteins through mitochondrial networks of different architectures [38].

Our quantitative calculations focus on a simplified dynamic system, with a single source of material held at fixed concentration. Realistic biological scenarios are of course likely to involve additional complications, including multiple sources (such as the mitochondrial nucleoids), non-trivial regulation at the source, or diffusive barriers within the mitochondria [63]. We also assumed that individual mitochondrial units are all identical in their fusion and fission behavior, whereas it is possible that some units remain isolated from the rest of the network, while others are more likely to engage in interactions. Furthermore, dynamic rearrangements beyond fusion and fission (such as tubule extension and branch sliding) may contribute to mixing within individual mitochondrial network components [76–78]. However, the minimal model presented here provides a basic building block from which more complicated scenarios can be constructed and which can serve as a null hypothesis for analyzing experimental observations.

This work brings us closer to understanding the functional implications of variable network connectivity for the spread of ions, lipids, proteins, and genetic information within mitochondria. For example, diffusive spreading dictates the heterogeneity of mitochondrial contents arising from mRNA and protein import site localization on the mitochondrial surface [58, 79]. Similarly, diffusion of mitochondrial transcription factors and mRNAs may dictate the spheres of influence of individual nucleoids within the network [80].

Mitochondrial networks are known to alter their architecture in response to changing environmental conditions, with excess glucose causing network fragmentation while starvation results in hyperfused networks [38]. A quantitative framework for material spreading in different structures provides insight on the implications of these transitions for many biologically critical processes, such as the distribution of harmful reactive oxygen species [47], the ability to isolate or complement deleterious DNA mutations [80, 81], and the tunneling of calcium ions, proton gradients, and ATP throughout the cell [48, 49, 82].

While we have focused on mitochondria, analogous problems of diffusive spreading arise in many systems, such as porous media in the geosciences [23], trophallactic networks in honeybees [4], and Alzheimers progression across connected regions in the brain [83]. By bringing together models of static physical networks and transiently interacting social networks, our results enable a quantitatively predictive link from network architecture

to the rate of diffusive dispersion.

ACKNOWLEDGMENTS

EFK acknowledges funding from NSF grant PHYS-2310229, the Chan Zuckerberg Initiative, and a grant from the UCSD Academic Senate. SL acknowledges funding by CZI Metabolism Across Scales grant #RR-8817, and by NSF CAREER award #2339182. We are grateful to Austin EYT Lefebvre, Gabriel Sturm, Nigel Goldenfeld, and Suliana Manley and to the members of the CZI Theory Institute Without Walls for helpful discussions.

SUPPLEMENTAL APPENDIX

A. Exact solution for static physical networks

For a stationary network structure, the total material content at steady-state can be computed analytically by solving the diffusion equation on each linear segment, then linking these solutions together at the junctions. The segment containing a source unit is separated into two segments on either side of the source. The diffusion equation and corresponding boundary conditions for each segment is:

$$\begin{aligned} D_p \frac{d^2 c_n(x)}{dx^2} - k_d c_n(x) &= 0, \\ c_{n_1^i}(x_{n_1^i}) &= c_{n_2^i}(x_{n_2^i}) = c_{n_3^i}(x_{n_3^i}), \\ \sum_{j=1}^{\deg(i)} \frac{dc_{n_j^i}}{dx} \Big|_{x_{n_j^i}} &= 0 \end{aligned} \quad (5)$$

where n_j^i is the j -th edge connected to node i and $x_{n_j^i}$ is the value of x on that edge at node i . For each segment, $0 < x < \ell_{n_j^i}$ and $x_{n_j^i} \in \{0, \ell_{n_j^i}\}$, where $\ell_{n_j^i}$ is the segment length. The middle equation defines continuity of the concentration fields, and the final equation conserves flux. This system has general solutions:

$$c_n(x) = A_n \cosh(x/\lambda_p) + B_n \sinh(x/\lambda_p)$$

allowing us to rewrite the boundary conditions as a large matrix equation $M\vec{\alpha} = \vec{v}$, where $\vec{\alpha}$ is a stacked vector of coefficients A_n, B_n , and \vec{v} is zero except for boundaries of the source unit. The total material in the network is found by integrating along all segments m outside of the source unit, to yield $S = \sum_m \int_0^{\ell_m} c_m(x) dx$.

Because the material delivered will depend on the choice of source unit within the network, we repeat this procedure for all possible choices of source unit and average the values of S . This result is then averaged over each replicate snapshot to give the exact solution (solid curves in Fig. 2).

B. Continuum Approximation for Static Physical Networks

We model highly-connected, stationary, physical network structures as an effective d -dimensional sphere through which diffusive material spreads from a localized source.

1. Selection of the effective domain size R_n

To extract the appropriate size of the continuum domain, we use the dimension d and the mean graph distance between pairs of nodes $\langle r_g \rangle$ in a given network. As we are approximating the network by a d -dimensional sphere, the mean distance between points in that sphere [84] should be equal to the mean graph distance. This yields the relationship:

$$R_n = \frac{(2d+1)\langle r_g \rangle}{2d\beta_d}, \quad (6)$$

$$\beta_d = \frac{2^{d+1}\Gamma(d+1)^3}{(d+1)\Gamma(\frac{d+1}{2})^2\Gamma(2d+1)}$$

However, for dimension less than 2, where diffusive search is compact and geometry-dependent [85], the position of the source within the domain becomes important.

For the linear case ($d=1$), specifically, a source point selected at random on a line of length $2R_n$, will on average be a distance $R_n/2$ from the nearest end. The steady-state distribution profile from this source can be solved analytically to give the total amount delivered:

$$S = \frac{\lambda_p}{\ell_0} \left[\tanh\left(\frac{R_n}{2\lambda_p}\right) + \tanh\left(\frac{3R_n}{2\lambda_p}\right) \right] \quad (7)$$

An alternate approach is to solve for $S^{(1)}$: the material delivered from a central source in a linear domain of radius $R^{(1)} = R_n/2$, and separately $S^{(2)}$: material delivered from a central source in a domain of radius $R^{(2)} = 2R_n - R_n/2$. Averaging these results together gives the exact expression in Eq. 7.

Analogously, for the d -dimensional case, a source point selected at random in a hypersphere of radius R_n will be at a distance of $R^{(1)} = 1/(d+1)R_n$ from the boundary. We compute $S^{(1)}$: the total material delivered from a central source in a hypersphere of radius $R^{(1)}$. Separately, we compute the result $S^{(2)}$ for a hypersphere of radius $(R^{(2)})^d = 2(R_n)^d - (R^{(1)})^d$. The average d -dimensional volume of the two hyperspheres is thus equal to the total volume. The two resulting solutions for delivered material are averaged together to give $S = (S^{(1)} + S^{(2)})/2$. Although this is not an exact solution for $d > 1$, it provides a good approximation for material delivery in simulated networks, where source points are selected uniformly to start anywhere on the network (Fig. 2, dashed-square curves).

2. Solving the continuum d -dimensional model (Eq. 1)

Starting with the general solution for the concentration [72]:

$$c(r) = Ax^\nu I_\nu(x) + Bx^\nu K_\nu(x) \quad (8)$$

we first apply the boundary conditions to solve for the constants A, B as follows. The reflecting outer boundary sets:

$$\left. \frac{dc}{dr} \right|_{R_n} = \frac{\sqrt{d}}{\lambda_p} \left. \frac{dc}{dx} \right|_{x_2} = Ax_2^\nu I_{\nu-1}(x_2) - Bx_2^\nu K_{\nu-1}(x_2) = 0$$

$$\rightarrow \frac{B}{A} = \frac{I_{\nu-1}(x_2)}{K_{\nu-1}(x_2)} \quad (9)$$

and the fixed-concentration inner boundary sets:

$$c(a_n) = c(x_1) = C_0^{(d)} = A \left(x_1^\nu I_\nu(x_1) + \frac{B}{A} x_1^\nu K_\nu(x_1) \right)$$

$$\rightarrow A = \frac{C_0^{(d)} x_1^{-\nu}}{I_\nu(x_1) + \frac{B}{A} K_\nu(x_1)}, \quad (10)$$

where $C_0^{(d)}$ is related to the linear concentration of the fixed unit, h_0 , as $M_d a_n^d C_0^{(d)} = \ell_0 h_0 = 1$, and M_d is the volume of a d -dimensional unit sphere (i.e. $\frac{4}{3}\pi$ in 3D). The total material delivered is then found through integration of the concentration field over space:

$$S_d = U_d \int_{a_n}^{R_n} r^{d-1} c(r) dr = U_d \left(\frac{\lambda_p}{\sqrt{d}} \right)^d \int_{x_1}^{x_2} x^{d-1} c(x) dx$$

$$= U_d \left(\frac{\lambda_p}{\sqrt{d}} \right)^d A \left[-x_1^{1-\nu} \left(I_{\nu-1}(x_1) - \frac{B}{A} K_{\nu-1}(x_1) \right) \right] \quad (11)$$

where U_d is surface area of a d -dimensional unit sphere (i.e. 4π in 3D) and the x_2 term vanishes by the outer boundary condition. Substituting in the definitions of $A, C_0^{(d)}$, and B/A we arrive at Eq. 1:

$$S_d = U_d \left(\frac{\lambda_p}{\sqrt{d}} \right)^d x_1^{1-2\nu} \left(\frac{1}{M_d a_n^d} \right) \frac{[-I_{\nu-1}(x_1) + \frac{B}{A} K_{\nu-1}(x_1)]}{[I_\nu(x_1) + \frac{B}{A} K_\nu(x_1)]}$$

$$= \frac{d}{x_1} \frac{[-I_{\nu-1}(x_1) + \frac{I_{\nu-1}(x_2)}{K_{\nu-1}(x_2)} K_{\nu-1}(x_1)]}{[I_\nu(x_1) + \frac{I_{\nu-1}(x_2)}{K_{\nu-1}(x_2)} K_\nu(x_1)]} \quad (12)$$

since U_d/M_d is simply the dimension d [86].

C. Mean-field model for social networks

For social networks consisting of identical diffusing units that exchange contents upon interaction, we develop a continuum field-based model for the spatial spreading of material. This model can apply to small clusters as well as completely fragmented units, so long as the material distribution within each cluster is approximately homogeneous.

1. *Model for spatial material concentration (Eq. 2)*

We derive the dynamic equation of a spatial mean concentration field, $h(\vec{r}, t)$, defined as the average material concentration per unit at position \vec{r} relative to the source cluster at time t . For uniform diffusing clusters in 3D, we assume spherical symmetry and express the concentration field as a function of the radial coordinate r . The material is carried by clusters with relative diffusivity D and decays at rate k_d , giving a simple reaction-diffusion equation for positions outside the contact zone ($r > b$):

$$\frac{dh(r, t)}{dt} = D\nabla^2 h(r, t) - k_d h(r, t) \quad (13)$$

Material exchange between non-source clusters has no effect on the average material concentration at the given position.

Two adjustments are made to Eq. 13 when clusters are within the contact volume v_c ($a < r < b$), where they are able to undergo fusion with the source cluster. First, we assume that the contact region is very thin relative to the domain size, so that the concentration field can be regarded as a spatially uniform value: $h_c(t)$. Material leaves the contact zone via diffusive flux through its outer boundary. This flux also forms the boundary condition at $r = b$ for Eq. 13. The spatial density of material is ρh , where ρ is the density of mitochondrial units. The overall current leaking out of the zone can then be expressed as:

$$I = -D\rho \left. \frac{dh(r, t)}{dr} \right|_b (4\pi b^2) \quad (14)$$

The per-unit loss of concentration is $I/(\rho v_c)$, as we must divide the total escaping concentration by the number of units in the contact volume.

An additional adjustment accounts for the injection of material into the network upon fusion through the term $+k_u(h_0\ell_0 - h_c)$, where k_u is the rate for each cluster to fuse with the source. This term arises from the fact that whenever a cluster fuses with the source cluster, both clusters leave the interaction with concentration $h_0 = 1/\ell_0$, meaning that the material per unit in the non-source cluster increases by $(h_0\ell_0 - h_c)$. With these modifications, we arrive at the dynamic equation for per-unit concentration within the contact zone:

$$\frac{dh_c(t)}{dt} = k_u(h_0\ell_0 - h_c(t)) - \frac{I}{\rho v_c} - k_d h_c(t) \quad (15)$$

At steady-state, the time derivatives in Eq. 13, 15 are set to 0 to solve for the spatial profile $h(r)$, as described below.

2. *Selection of the steric and contact radii, a, b and effective fusion rate, k_u*

The continuum model requires defining inner and outer radii a, b for interacting clusters. Since the inner radius

a represents a steric exclusion distance, we set $a = 2R_g$, where R_g is the average radius of gyration for clusters in the network. Rather than defining b directly, we set the total volume v_c available for fusion to a cluster by multiplying the average number of nodes available for fusion (those with degree below 3) by the contact volume per node. The contact volume per node describes the volume within which two individual nodes can undergo fusion; it is computed in detail in Ref. [57]. This procedure fixes b through the relationship $v_c = \frac{4}{3}\pi(b^3 - a^3)$.

The effective fusion rate is also dependent on the number of nodes available for fusion. In our simulations, we have separate orientation-dependent rates for tip-tip (between two degree-1 nodes) and tip-side (between a degree-1 and degree-2 node) fusion: $k_{u1}(\Theta)$ and $k_{u2}(\Theta)$. The effective rate k_u is calculated as a weighted sum of these two fusion types:

$$k_u = \langle k_{u1}(\Theta) \rangle \cdot x_1 \left(\frac{x_1}{x_1 + x_2} \right) + \langle k_{u2}(\Theta) \rangle \cdot \frac{2x_1x_2}{x_1 + x_2} \quad (16)$$

where the angle brackets denote averaging over orientations for a pair of nodes, given that they are close enough in space to fuse (within the contact volume per node) and x_1, x_2 denote the average number of degree 1 and 2 nodes per cluster, respectively. Since all nodes in the incoming cluster have a chance to fuse with the source cluster while inside v_c , the tip-tip rate is multiplied by the number of degree-1 nodes in the incoming cluster and the probability to be near a degree-1 node from the source cluster, given a position inside v_c . The tip-side rate is weighted analogously, but contains two contributions. First, we include the number of degree-1 nodes in the incoming cluster multiplied by the probability to be near a degree-2 node from the source cluster. Second, we have the number of degree-2 nodes in the incoming cluster multiplied by the probability to be near a degree-1 node from the source cluster. Further details of the fusion and fission model and its dependence on the orientation and position of interacting units can be found in Ref. [57].

3. *Solving the mean-field model (Eq. 2,3)*

We begin by writing down the general solution at steady-state, $h(r) = \frac{1}{r}(Ae^{r/\lambda} + Be^{-r/\lambda})$ where $\lambda = \sqrt{D/k_d}$, with D the relative cluster diffusivity. Applying the outer boundary condition gives:

$$\begin{aligned} \left. \frac{dh}{dr} \right|_R &= \frac{Ae^{R/\lambda} - Be^{-R/\lambda}}{R\lambda} - \frac{Ae^{R/\lambda} + Be^{-R/\lambda}}{R^2} = 0 \\ \rightarrow \frac{B}{A} &= e^{2R/\lambda} \left(\frac{R - \lambda}{R + \lambda} \right) \end{aligned} \quad (17)$$

and the inner continuity condition gives:

$$h(b) = \frac{A}{b} \left(e^{b/\lambda} + \frac{B}{A} e^{-b/\lambda} \right) = h_c \quad (18)$$

$$\rightarrow A = \frac{(R + \lambda) e^{-b/\lambda} b h_c}{(R + \lambda) + (R - \lambda) e^{2(R-b)/\lambda}}$$

Next we find the steady-state h_c by setting $\frac{dh_c}{dt} = 0$. First, solving for the current across the boundary gives:

$$\begin{aligned} \frac{I}{k_d \rho v_c} &= - \frac{4\pi b^2 \lambda^2}{v_c} \left. \frac{dh}{dr} \right|_b \\ &= - \frac{4\pi b^2 \lambda^2}{v_c} A \left(\frac{e^{b/\lambda} - \frac{B}{A} e^{-b/\lambda}}{b\lambda} - \frac{e^{b/\lambda} + \frac{B}{A} e^{-b/\lambda}}{b^2} \right) \\ &= h_c z / v_c \end{aligned} \quad (19)$$

where the last step comes from plugging in the results for A , $\frac{B}{A}$ and we define:

$$\frac{z}{4\pi b \lambda} = \frac{(\lambda - b)(R + \lambda) + (\lambda + b)(R - \lambda) e^{2(R-b)/\lambda}}{(R + \lambda) + (R - \lambda) e^{2(R-b)/\lambda}} \quad (20)$$

Now solving for h_c directly:

$$\begin{aligned} k_u(1 - h_c) - I/\rho v_c - k_d h_c &= 0 \\ h_c(1 + k_u/k_d + z/v_c) &= k_u/k_d \\ h_c &= \frac{k_u/k_d}{1 + k_u/k_d + z/v_c} \end{aligned} \quad (21)$$

The total concentration outside of the fixed cluster is then given by:

$$\begin{aligned} S &= (N_0 - \langle n \rangle) \frac{4\pi \left(\int_a^b r^2 h_c dr + \int_b^R r^2 h(r) dr \right)}{4\pi \int_a^R r^2 dr} \\ &= \rho \left(h_c v_c + 4\pi A \left[(r\lambda - \lambda^2) e^{r/\lambda} - \frac{B}{A} (r\lambda + \lambda^2) e^{-r/\lambda} \right]_b^R \right) \\ &= \rho h_c (v_c + z) \end{aligned} \quad (22)$$

as in Eq. 3. To get the total concentration including the fixed cluster, we add the the material per unit at the source ($h_0 \ell_0 = 1$) multiplied by the size of the fixed cluster, ($\langle n \rangle - 1$) (ignoring the fixed unit itself). The limiting behaviors for short τ_d , τ_{enc} , and τ_u (indicated in Fig. 3) are each derived straightforwardly through expansion of z for small $\lambda \ll R$.

D. Time-dependent spread of material without decay

The results in the main text focus on the total material delivered to a network at steady-state, where such a state is reached through a balance of spreading and decay. Simulations and analytical approximations provide

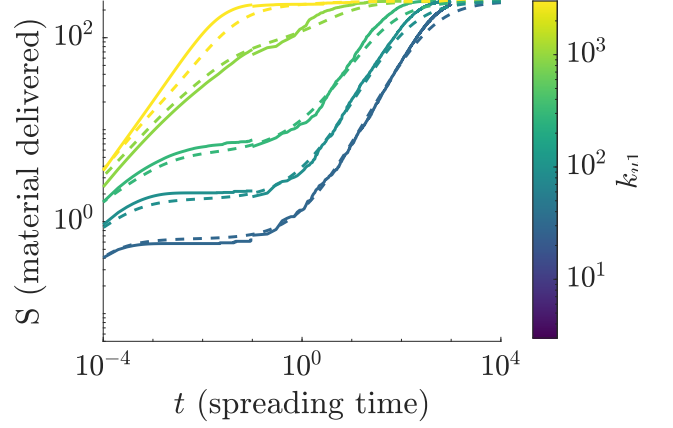


FIG. S1. The total material in the network plotted as a function of time for a system with no material decay, with $S(t=0) = 0$. Solid lines correspond to simulated networks, filling with material over time. Simulation parameters are identical to Fig. 4 but with $k_d = 0$. Dashed curves give the combined analytic steady-state solution for physical and social networks, as in Fig. 4, plotted with $t = \tau_d$ as the effective spreading time.

a comprehensive picture for this system (Fig. 4). The decay rate k_d in this model plays the role of setting the timescale on which spreading is being considered.

To show the generality of the analytic approximations, we consider the related problem of time-dependent spreading without decay. With $k_d = 0$, there is no steady-state but we can instead quantify the temporal evolution of material content in the network: $S(t)$. To probe this question, we run simulations using the same parameters as in Fig. 4 with $k_d = 0$, tracking the total material delivered to the network over time. Fig. S1 shows that the combined steady-state analytical solution (Eq. 4), provides a good approximation to the time-dependent spreading $S(t)$ when evaluated using the corresponding effective decay rate: $k_d = 1/t$.

E. Simulation Methods

1. Dynamic network simulations

We start with the dynamic network simulation framework described in [57]. Edge-units are spherocylinders with length $\ell_0 = 0.5$ and have steric exclusion radius $r_s = 0.15$. All $N_0 = 250$ units are confined by a reflecting domain boundary of radius $R = 5$. To generate the network structures, we use variable tip-tip and tip-side fusion rate constants k_{u1}, k_{u2} as indicated in the text, with the fission rate constant set to $k_f = 1$ to normalize time units throughout. Fusion between two nodes can occur when the nodes are separated by less than $2r_c$, where $r_c = 0.2$ is the contact radius. Random motion of units and clusters is realized by a diffusivity of 1 applied

at each node, giving $D_1 \approx 0.5$ per isolated unit. Assuming a fission rate on the order of $k_f = 1/(2\text{min})$, this dimensionless diffusivity corresponds to approximately $D_1 \approx 0.25\mu\text{m}^2/\text{min}$.

Diffusion of material through the network is accomplished using finite-volume simulations built on top of the dynamic network simulation. Material concentration fields are discretized on a per-unit basis, with the change in concentration across each junction (node) in the network calculated as:

$$\frac{dc_{n_j^i}}{dt} = \frac{D_p}{\ell_0^2} \sum_{k=1}^{\text{deg}(i)} (c_{n_k^i} - c_{n_j^i}) \quad (23)$$

where $D_p = 4800$ is the default particle diffusivity and $c_{n_j^i}$ is the per-unit concentration on the j -th edge connected to node i . Material exchange is thus only possible across connected (fused) units. Decay is applied uniformly across the network as $dc/dt = -k_d c$. The simulations proceed through forward Euler stepping with a timestep of $\Delta t = 10^{-4}$. After allowing the network structure to equilibrate for 2×10^6 simulation steps, we initialize the concentration of all units at $c = 0$, except for one source unit chosen at random, whose per-unit concentration is fixed to $c = \ell_0 h_0 = 1$. We then run each spreading simulation for at least 5 times the decay time ($5\tau_d$), averaging the total material over the second half of the simulation. We further average over 9 choices of the source node per simulation and at least 3 independent simulation replicates.

2. Interacting spheres simulations for social networks

For simulations of the simplified model for highly fragmented mitochondria, we take an agent-based approach with $N_0 = 251$ identical spherical units of steric exclusion radius $a/2 = 0.15$. These spherical units are initially distributed uniformly inside a reflecting spherical boundary of radius $R = 5$ and are allowed to diffuse with diffusivity $D_1 = 0.5$. One unit is selected as the source and is assigned constant concentration $c = 1$. Transient fusion between two units occurs at rate k_u whenever the centers of the spheres are separated by less than b , where $b = 0.4$ represents the contact distance. Upon fusion, the sphere concentrations c_1, c_2 are updated to $c'_1 = c'_2 = (c_1 + c_2)/2$ to represent equilibration. Fusions are immediately followed by fission. If a non-source unit fuses with the source unit, its concentration is raised to $c = 1$. Decay is applied uniformly across the non-source units with $c(t + \Delta t) = c(t)e^{-\Delta t/\tau_d}$ where the timestep $\Delta t = 10^{-2} \cdot \min(10^{-1}, k_u^{-1}, \tau_d)$. We run each simulation until the simulation time is at least $t = 50$ for $\tau_d \leq 1$ and at least $t = 2000$ for $\tau_d > 1$, and average the total material over the last quarter of the simulation.

F. Experimental Imaging and Data Processing

1. Mammalian cell growth, transfection, and vital dyes

Human IMR90 cells (American Type Culture Collection #CCL-186) and U2OS-Cas9 cells (HD Cas9-012) were grown in high-glucose Dulbecco's modified Eagle's medium (DMEM) supplemented with 10% heat-inactivated fetal bovine serum, 1% L-Glutamine (100X), and 1% penicillin/streptomycin at 37°C in a humidified 5% CO₂ chamber. Human SH-SY5Y cells (American Type Culture Collection #CRL-2266) were grown in high glucose Dulbecco's modified Eagle's medium (DMEM) supplemented with 10% heat-inactivated fetal bovine serum, 1% non essential amino acids (NEAA) and 1% Sodium Pyruvate (NaPyr) at 37°C in a humidified 5% CO₂ chamber. Before imaging, cells were seeded onto glass-bottom 35-mm dishes (Mattek) and cultured for 24 to 48 hours. Transient transfection was performed using Lipofectamine 2000 according to the manufacturer's protocol (Thermo Fisher Scientific) and cells were imaged 24 hours later, unless otherwise noted. U2OS-Cas9 cells were transfected with non-targeting Scrambled sgRNA#1 (EditCo) using RNAiMAX Transfection Reagent according to the manufacturer's protocol (Thermo Fisher Scientific), media was replaced 24 hours later, and cells imaged 5 days later. For live cell imaging, 1 ml of conditioned cell media was removed and reserved prior to staining with 50 nM MitoTracker Deep Red (Thermo Fisher Scientific) directly in the imaging dish for 30 min. Medium was then replaced with the reserved conditioned media just before imaging. Plasmids and resource identifiers are reported in Table I.

Plasmid	Source and Reference
Mito-BFP	mito-BFP was a gift from Gia Voeltz (Addgene plasmid # 49151; http://n2t.net/addgene:49151 ; RRID:Addgene.49151). https://pubmed.ncbi.nlm.nih.gov/21885730/
Su9-EGFP	Su9-EGFP was a gift from David Chan (Addgene plasmid # 23214; http://n2t.net/addgene:23214 ; RRID:Addgene.23214). https://pubmed.ncbi.nlm.nih.gov/12527753/

TABLE I. Plasmids

2. Microscopy and image acquisition

All images were acquired using a Zeiss LSM 980 with Airyscan 2 laser scanning confocal microscope, equipped with 405-nm, 488-nm, 561-nm, and 639-nm laser lines and Fast Airyscan detector array. Images were acquired using an inverted 63x/1.4 numerical aperture oil objective. All live imaging was done in a humidified chamber at 37°C and in the presence of 5% CO₂. Airyscan process-

ing was performed using Zeiss ZEN Blue software version 3.7 (Carl Zeiss). Image brightness and/or contrast were linearly adjusted in ZEN Blue.

3. Network Extraction

Individual cells are separated and manually cropped in ImageJ using a max projection in Z and time. Areas and volumes are estimated by measuring the cell area and subtracting the nuclear area, with height assumed uniform throughout. The mitochondria for each cell are segmented and tracked using the software package Nellie [87]. Skeletons and corresponding network structures are extracted from the Nellie segmentation at each time point using the skimage [88] and skan [89] python packages. Degree distributions for the network are computed as in [57] to provide for an assumed underlying mitochondrial unit length of $0.5\mu\text{m}$, matching simulations. We then extract all structural parameters (cluster sizes, radius of gyration, fractal dimension, mean graph distance, etc.) for each imaged network in the same way as for simulated networks, using a custom network analysis package in Matlab [90].

4. Dynamic measurements

There are two dynamic parameters which must be extracted from experimental data in order to apply the analytic model. From Nellie outputs of segmented and time-linked objects, we extract the trajectories of individual labeled mitochondria, as marked by their center-of-mass positions in consecutive frames. Trajectories containing fewer than three time points or very fast motion of greater than $0.64\mu\text{m/s}$ are discarded. We restrict our analysis to mitochondria of length $2\mu\text{m}$ or less, as large clusters are more prone to tracking artifacts. Positions are projected into the xy-plane and mean squared displacements (MSD) are calculated between consecutive frames on each trajectory. Finally, the effective mitochondrial diffusivity for a given cell is estimated as: $D_{\text{mito}} = \langle \Delta r^2 \rangle / (4\Delta t)$, where $\langle \Delta r^2 \rangle$ is the MSD between consecutive frames and Δt is the time between frames.

Second, fission events are manually identified in ImageJ using the max projection in Z for each cell. To calculate the effective per-node fission rate constant, k_f , we then divide these fission counts by the elapsed time for the movie and a weighted sum of junction nodes ($x_2 + \frac{3}{2}x_3$), with x_i the average number of degree- i nodes in the network [13].

It is important to make a distinction between microscopic fusion and fission events, which occur with local rate constants k_f, k_u , and large-scale events that encompass network rearrangement. The latter include ‘novel fusions’ (fusion with a new network unit) and ‘complete fission’ events that proceed them. As found in [57], for simulated mitochondrial networks, the complete fission

rate constant is roughly ten-fold lower than the local fission rate constant k_f . Because microscopic fissions are quickly followed by re-fusion and are unlikely to be observed in our time-lapse images, we assume these counts correspond to complete fission events only, and set k_f to be ten-fold higher than the observed rate. Finally, the cluster-cluster fusion rate k_u is estimated as $k_u \approx \langle k_f \rangle (C_1/\delta v_1 + C_2/\delta v_2)$ where $C_1 = V_{\text{cell}}x_2/(\frac{1}{2}x_1^2)$, $C_2 = \frac{3}{2}V_{\text{cell}}x_3/(x_1x_2)$, and $\delta v_1, \delta v_2$ are the contact volumes per node for tip-tip and tip-side fusion [13, 57].

We note that our estimates for the local fission rate are likely an underestimate, as we are limited by framerate and the ability to manually identify all fission events within a given movie. Estimates for the mitochondrial diffusivity, on the other hand, are likely a slight overestimate, as tracking artifacts may cause artificial jumps in trajectories which cannot be completely filtered out. However, these limitations do not alter the results plotted in Fig. 5b,d because the mitochondria in these cells are already in a mobility-limited regime. This means that when spreading occurs via cluster-cluster interactions as described by the social network model, the interaction time is dominated by the timescale to encounter new clusters, τ_{enc} .

We can see quantitatively that the mitochondria in our data set fall into this regime by analyzing the ratio: $\tau_{\text{enc}}/\tau_u = \rho v_c k_u / (\rho 4\pi D b)$, which compares the total fusion rate in the contact zone to the rate of mitochondria arriving at the contact zone. For the cells in our data set, this ratio ranges from $10^1 - 10^4$, with the majority of cells centered around 10^2 . Because our estimate for k_u is a lower bound and our estimate for D is an upper bound, the predicted ratio of τ_{enc}/τ_u must also be a lower bound. Therefore we can safely say that the results for spreading in the mitochondrial networks used for this analysis are insensitive to potential inaccuracy in the measured fission rate.

5. Solving the social network model in a slab-like geometry

As the cells we are analyzing are nearly flat (area $\sim 1000\mu\text{m}^2$, height $\sim 2\mu\text{m}$), we solved the social model (Eq. 2) in a quasi-2D slablike geometry to make the predictions shown in Fig. 5. This amounts to solving the diffusion equation in cylindrical coordinates, with a result that looks exactly the same as Eq. 3 up to a redefinition of the spatial spreading term, contact volume, and mitochondrial unit density:

$$\frac{z}{2\pi b H \lambda} = \frac{-I_1(b/\lambda)K_1(R/\lambda) + K_1(b/\lambda)I_1(R/\lambda)}{I_0(b/\lambda)K_1(R/\lambda) + K_0(b/\lambda)I_1(R/\lambda)}, \quad (24a)$$

$$v_c = \pi(b^2 - a^2)H, \quad (24b)$$

$$\rho = (N_0 - \langle n \rangle) / [\pi(R^2 - a^2)H], \quad (24c)$$

where I_j, K_j are modified Bessel functions, H is the height of the cell and we calculate $R = \sqrt{A_{\text{cell}}/\pi}$, the effective planar radius of the cell based on the measured

cell area. The steric radius a is set based on the radius of gyration averaged over all clusters and b is calculated from Eq. 24b, analogously to the 3D simulations.

In 4 of the analyzed SH-SY5Y cells, the average mitochondrial cluster size was greater than half of the total mitochondrial content in the cell. As the social network model assumes multiple interacting clusters of similar size, we used only the stationary network approximation to estimate the spreading times for these networks, with the source assumed to be located on a cluster of the typical largest size (for these networks, ~ 0.75 of the total mitochondrial content).

Supplemental Video Caption

Supplemental Video 1: Steady-state dynamics

of the mitochondrial network model. Material concentration is indicated on a white-to-red gradient. A single fixed-concentration unit serves as the source. Top: disconnected network, Middle: network near percolation transition, Bottom: hyperfused network. Simulation parameters correspond to those listed in Fig. 1b. Each movie runs over a simulated time of 60 dimensionless units (corresponding to ≈ 120 min).

Supplemental Video 2: Example live-cell imaging data of mitochondrial networks in SH-SY5Y (top), IMR90 (middle), and U2OS (bottom) cells. Raw (white) and segmented (multicolored) mitochondria are shown, with all segmentations obtained using Nellie [87]. Connected clusters are indicated by different colors in the initial frame, with subsequent voxel colors determined via Nellie's flow mapping algorithm. All movies run backward then forward over a span of 116 seconds.

-
- [1] A. J. Tatem, D. J. Rogers, and S. I. Hay, Global transport networks and infectious disease spread, *Adv Parasit* **62**, 293 (2006).
- [2] M. E. Newman, Spread of epidemic disease on networks, *Phys Rev E* **66**, 016128 (2002).
- [3] A. Montanari and A. Saberi, The spread of innovations in social networks, *P Natl Acad Sci* **107**, 20196 (2010).
- [4] T. Gernat, V. D. Rao, M. Middendorf, H. Dankowicz, N. Goldenfeld, and G. E. Robinson, Automated monitoring of behavior reveals bursty interaction patterns and rapid spreading dynamics in honeybee social networks, *P Natl Acad Sci* **115**, 1433 (2018).
- [5] B. Blonder and A. Dornhaus, Time-ordered networks reveal limitations to information flow in ant colonies, *PLoS one* **6**, e20298 (2011).
- [6] J. P. Kinney, J. Spacek, T. M. Bartol, C. L. Bajaj, K. M. Harris, and T. J. Sejnowski, Extracellular sheets and tunnels modulate glutamate diffusion in hippocampal neuropil, *J Comp Neurol* **521**, 448 (2013).
- [7] E. Syková and C. Nicholson, Diffusion in brain extracellular space, *Physiol Rev* **88**, 1277 (2008).
- [8] P. R. King, J. S. Andrade Jr, S. V. Buldyrev, N. Dokholyan, Y. Lee, S. Havlin, and H. E. Stanley, Predicting oil recovery using percolation, *Physica A: Statistical mechanics and its Applications* **266**, 107 (1999).
- [9] M. Barthélemy, Spatial networks, *Phys Rep* **499**, 1 (2011).
- [10] N. Dehmamy, S. Milanlouei, and A.-L. Barabási, A structural transition in physical networks, *Nature* **563**, 676 (2018).
- [11] M. Pósfai, B. Szegedy, I. Bačić, L. Blagojević, M. Abért, J. Kertész, L. Lovász, and A.-L. Barabási, Impact of physicality on network structure, *Nat Phys* **20**, 142 (2024).
- [12] L. Blagojević and M. Pósfai, Three-dimensional shape and connectivity of physical networks, *Sci Rep* **14**, 16874 (2024).
- [13] V. M. Sukhorukov, D. Dikov, A. S. Reichert, and M. Meyer-Hermann, Emergence of the mitochondrial reticulum from fission and fusion dynamics, *PLoS Comput Biol* **8**, e1002745 (2012).
- [14] M. R. Islam, G. Tudryn, R. Bucinell, L. Schadler, and R. Picu, Morphology and mechanics of fungal mycelium, *Sci Rep* **7**, 13070 (2017).
- [15] C. S. Xu, M. Januszewski, Z. Lu, S.-y. Takemura, K. J. Hayworth, G. Huang, K. Shinomiya, J. Maitin-Shepard, D. Ackerman, S. Berg, *et al.*, A connectome of the adult drosophila central brain, *BioRxiv*, 2020 (2020).
- [16] Y. Ju, J. Zheng, M. Epstein, L. Sudak, J. Wang, and X. Zhao, 3d numerical reconstruction of well-connected porous structure of rock using fractal algorithms, *Comput Method Appl M* **279**, 212 (2014).
- [17] F. R. Chung, *Spectral graph theory*, Vol. 92 (American Mathematical Soc., 1997).
- [18] N. Masuda, M. A. Porter, and R. Lambiotte, Random walks and diffusion on networks, *Phys Rep* **716**, 1 (2017).
- [19] G. Pete, Á. Timár, S. Ö. Stefánsson, I. Bonamassa, and M. Pósfai, Physical networks as network-of-networks, *Nat Commun* **15**, 4882 (2024).
- [20] J. Hermon and P. Sousi, A comparison principle for random walk on dynamical percolation, *Ann Probab* **48**, 2952 (2020).
- [21] P. Chuphal, J. D. Lanctôt, S. P. Cornelius, and A. I. Brown, Mitochondrial network branching enables rapid protein spread with slower mitochondrial dynamics, *PRX Life* **2**, 043005 (2024).
- [22] P. Holme and J. Saramäki, Temporal networks, *Phys Rep* **519**, 97 (2012).
- [23] E. Herrera-Hernández, M. Coronado, and H. Hernández-Coronado, Fractal continuum model for tracer transport in a porous medium, *Physical Review E—Statistical, Nonlinear, and Soft Matter Physics* **88**, 063004 (2013).
- [24] Z. C. Scott, K. Koning, M. Vanderwerp, L. Cohen, L. M. Westrate, and E. F. Koslover, Endoplasmic reticulum network heterogeneity guides diffusive transport and kinetics, *Biophys J* **122**, 3191 (2023).
- [25] C. C. Crapart, Z. C. Scott, T. Konno, A. Sharma, P. Parutto, D. M. Bailey, L. M. Westrate, E. Avezov, and E. F. Koslover, Luminal transport through intact endoplasmic reticulum limits the magnitude of localized Ca^{2+} signals, *P Natl Acad Sci* **121**, e2312172121 (2024).
- [26] H. M. York, K. Joshi, C. S. Wright, L. Z. Kreplin, S. J.

- Rodgers, U. K. Moorthi, H. Gandhi, A. Patil, C. A. Mitchell, S. Iyer-Biswas, *et al.*, Deterministic early endosomal maturation emerges from a stochastic trigger-and-convert mechanism, *Nat Commun* **14**, 4652 (2023).
- [27] S. E. Cason, S. S. Mogre, E. L. Holzbaur, and E. F. Koslover, Spatiotemporal analysis of axonal autophagosome-lysosome dynamics reveals limited fusion events and slow maturation, *Mol Biol Cell* **33**, ar123 (2022).
- [28] Z. Wang, P. Natekar, C. Tea, S. Tamir, H. Hakozaki, and J. Schöneberg, MitoTNT: Mitochondrial temporal network tracking for 4D live-cell fluorescence microscopy data, *PLoS Comput Biol* **19**, e1011060 (2023).
- [29] M. P. Viana, A. I. Brown, I. A. Mueller, C. Goul, E. F. Koslover, and S. M. Rafelski, Mitochondrial fission and fusion dynamics generate efficient, robust, and evenly distributed network topologies in budding yeast cells, *Cell Syst* **10**, 287 (2020).
- [30] M. A. Aon, S. Cortassa, and B. O’Rourke, Percolation and criticality in a mitochondrial network, *P Natl Acad Sci* **101**, 4447 (2004).
- [31] J. M. Chustecki, D. J. Gibbs, G. W. Bassel, and I. G. Johnston, Network analysis of arabidopsis mitochondrial dynamics reveals a resolved tradeoff between physical distribution and social connectivity, *Cell Syst* **12**, 419 (2021).
- [32] H. Chen and D. C. Chan, Mitochondrial dynamics-fusion, fission, movement, and mitophagy-in neurodegenerative diseases, *Hum Mol Genet* **18**, R169 (2009).
- [33] F. Burté, V. Carelli, P. F. Chinnery, and P. Yu-Wai-Man, Disturbed mitochondrial dynamics and neurodegenerative disorders, *Nat Rev Neurol* **11**, 11 (2015).
- [34] W. Wang, F. Zhao, X. Ma, G. Perry, and X. Zhu, Mitochondria dysfunction in the pathogenesis of alzheimer’s disease: Recent advances, *Mol Neurodegener* **15**, 1 (2020).
- [35] J.-S. Park, R. L. Davis, and C. M. Sue, Mitochondrial dysfunction in parkinson’s disease: new mechanistic insights and therapeutic perspectives, *Curr Neurol Neurosci* **18**, 1 (2018).
- [36] M. Filosto, M. Scarpelli, M. S. Cotelli, V. Vielmi, A. Todeschini, V. Gregorelli, P. Tonin, G. Tomelleri, and A. Padovani, The role of mitochondria in neurodegenerative diseases, *J Neurol* **258**, 1763 (2011).
- [37] A. Izzo, M. Nitti, N. Mollo, S. Paladino, C. Procaccini, D. Faicchia, G. Cali, R. Genesio, F. Bonfiglio, R. Ciciello, *et al.*, Metformin restores the mitochondrial network and reverses mitochondrial dysfunction in down syndrome cells, *Hum Mol Genet* **26**, 1056 (2017).
- [38] M. Liesa and O. S. Shirihai, Mitochondrial dynamics in the regulation of nutrient utilization and energy expenditure, *Cell Metab* **17**, 491 (2013).
- [39] A. S. Rambold, B. Kostecky, N. Elia, and J. Lippincott-Schwartz, Tubular network formation protects mitochondria from autophagosomal degradation during nutrient starvation, *P Natl Acad Sci* **108**, 10190 (2011).
- [40] T. Kichuk, S. Dhamankar, S. Malani, W. A. Hofstadter, S. A. Wegner, I. M. Cristea, and J. L. Avalos, Using miter for 3d analysis of mitochondrial morphology and er contacts, *Cell Reports Methods* **4** (2024).
- [41] D.-F. Suen, K. L. Norris, and R. J. Youle, Mitochondrial dynamics and apoptosis, *Gene Dev* **22**, 1577 (2008).
- [42] J. R. Hom, J. S. Gewandter, L. Michael, S.-S. Sheu, and Y. Yoon, Thapsigargin induces biphasic fragmentation of mitochondria through calcium-mediated mitochondrial fission and apoptosis, *J Cell Physiol* **212**, 498 (2007).
- [43] P. Mishra and D. C. Chan, Mitochondrial dynamics and inheritance during cell division, development and disease, *Nat Rev Mol Cell Bio* **15**, 634 (2014).
- [44] K. Mitra, C. Wunder, B. Roysam, G. Lin, and J. Lippincott-Schwartz, A hyperfused mitochondrial state achieved at g1-s regulates cyclin e buildup and entry into s phase, *P Natl Acad Sci* **106**, 11960 (2009).
- [45] H. Chen, M. Vermulst, Y. E. Wang, A. Chomyn, T. A. Prolla, J. M. McCaffery, and D. C. Chan, Mitochondrial fusion is required for mtdna stability in skeletal muscle and tolerance of mtdna mutations, *Cell* **141**, 280 (2010).
- [46] A. Kowald and T. B. Kirkwood, Evolution of the mitochondrial fusion-fission cycle and its role in aging, *P Natl Acad Sci* **108**, 10237 (2011).
- [47] T. Yu, J. L. Robotham, and Y. Yoon, Increased production of reactive oxygen species in hyperglycemic conditions requires dynamic change of mitochondrial morphology, *P Natl Acad Sci* **103**, 2653 (2006).
- [48] H. Hoitzing, I. G. Johnston, and N. S. Jones, What is the function of mitochondrial networks? a theoretical assessment of hypotheses and proposal for future research, *Bioessays* **37**, 687 (2015).
- [49] V. P. Skulachev, Mitochondrial filaments and clusters as intracellular power-transmitting cables, *Trends Biochem Sci* **26**, 23 (2001).
- [50] T. Kleele, T. Rey, J. Winter, S. Zaganelli, D. Mahecic, H. Perreten Lambert, F. P. Ruberto, M. Nemir, T. Wai, T. Pedrazzini, *et al.*, Distinct fission signatures predict mitochondrial degradation or biogenesis, *Nature* **593**, 435 (2021).
- [51] P. K. Patel, O. Shirihai, and K. C. Huang, Optimal dynamics for quality control in spatially distributed mitochondrial networks, *Plos Comput Biol* **9**, e1003108 (2013).
- [52] I. Kim, S. Rodriguez-Enriquez, and J. J. Lemasters, Selective degradation of mitochondria by mitophagy, *Arch Biochem Biophys* **462**, 245 (2007).
- [53] G. Twig, A. Elorza, A. J. Molina, H. Mohamed, J. D. Wikstrom, G. Walzer, L. Stiles, S. E. Haigh, S. Katz, G. Las, *et al.*, Fission and selective fusion govern mitochondrial segregation and elimination by autophagy, *Embo J* **27**, 433 (2008).
- [54] J. Ngo, C. Osto, F. Villalobos, and O. S. Shirihai, Mitochondrial heterogeneity in metabolic diseases, *Biology* **10**, 927 (2021).
- [55] K. W. Ryu, T. S. Fung, D. C. Baker, M. Saoi, J. Park, C. A. Febres-Aldana, R. G. Aly, R. Cui, A. Sharma, Y. Fu, *et al.*, Cellular atp demand creates metabolically distinct subpopulations of mitochondria, *Nature* , 1 (2024).
- [56] A. I. Brown, L. M. Westrate, and E. F. Koslover, Impact of global structure on diffusive exploration of organelle networks, *Sci Rep* **10**, 4984 (2020).
- [57] K. B. Holt, J. Winter, S. Manley, and E. F. Koslover, Spatiotemporal modeling of mitochondrial network architecture, *PRX Life* **2**, 043002 (2024).
- [58] A. H. Khan, X. Gu, R. J. Patel, P. Chuphal, M. P. Viana, A. I. Brown, B. M. Zid, and T. Tsuboi, Mitochondrial protein heterogeneity stems from the stochastic nature of co-translational protein targeting in cell senescence, *Nat Commun* **15**, 8274 (2024).

- [59] J. C. Landoni, T. Kleele, J. Winter, W. Stepp, and S. Manley, Mitochondrial structure, dynamics, and physiology: light microscopy to disentangle the network, *Annual Review of Cell and Developmental Biology* **40** (2024).
- [60] G. Csordás, P. Várnai, T. Golenár, S. Roy, G. Purkins, T. G. Schneider, T. Balla, and G. Hajnóczky, Imaging interorganelle contacts and local calcium dynamics at the er-mitochondrial interface, *Mol Cell* **39**, 121 (2010).
- [61] R. J. LeVeque, *Finite volume methods for hyperbolic problems*, Vol. 31 (Cambridge university press, 2002).
- [62] V. M. Sukhorukov and J. Bereiter-Hahn, Anomalous diffusion induced by cristae geometry in the inner mitochondrial membrane, *PLoS One* **4**, e4604 (2009).
- [63] C. E. Dieteren, S. C. Gielen, L. G. Nijtmans, J. A. Smeitink, H. G. Swarts, R. Brock, P. H. Willems, and W. J. Koopman, Solute diffusion is hindered in the mitochondrial matrix, *P Natl Acad Sci* **108**, 8657 (2011).
- [64] H. Rampelt, R. M. Zerbes, M. van der Laan, and N. Pfanner, Role of the mitochondrial contact site and cristae organizing system in membrane architecture and dynamics, *Biochimica et Biophysica Acta (BBA)-Molecular Cell Research* **1864**, 737 (2017).
- [65] V. M. Sukhorukov, D. Dikov, K. Busch, V. Strecker, I. Wittig, and J. Bereiter-Hahn, Determination of protein mobility in mitochondrial membranes of living cells, *Biochimica et Biophysica Acta (BBA)-Biomembranes* **1798**, 2022 (2010).
- [66] W. J. Koopman, F. Distelmaier, M. A. Hink, S. Verkaart, M. Wijers, J. Fransen, J. A. Smeitink, and P. H. Willems, Inherited complex i deficiency is associated with faster protein diffusion in the matrix of moving mitochondria, *Am J Physiol-cell Ph* **294**, C1124 (2008).
- [67] A. A. Gerencser and V. Adam-Vizi, Mitochondrial ca_2+ dynamics reveals limited intramitochondrial ca_2+ diffusion, *Biophys J* **88**, 698 (2005).
- [68] B. Corci, O. Hooiveld, A. M. Dolga, and C. Åberg, Extending the analogy between intracellular motion in mammalian cells and glassy dynamics, *Soft Matter* **19**, 2529 (2023).
- [69] G. Twig, X. Liu, M. Liesa, J. D. Wikstrom, A. J. Molina, G. Las, G. Yaniv, G. Hajnóczky, and O. S. Shirihai, Biophysical properties of mitochondrial fusion events in pancreatic β -cells and cardiac cells unravel potential control mechanisms of its selectivity, *Am J Physiol-cell Ph* **299**, C477 (2010).
- [70] R. G. Abrisch, S. C. Gumbin, B. T. Wisniewski, L. L. Lackner, and G. K. Voeltz, Fission and fusion machineries converge at er contact sites to regulate mitochondrial morphology, *J Cell Biol* **219**, e201911122 (2020).
- [71] O. Shanker, Defining dimension of a complex network, *Mod Phys Lett B* **21**, 321 (2007).
- [72] S. Redner, *A Guide to First-Passage Processes* (Cambridge University Press, 2001).
- [73] S. Logan, Effects of temperature on the rates of diffusion-controlled reactions, *T Faraday Soc* **63**, 1712 (1967).
- [74] M. P. Viana, S. Lim, and S. M. Rafelski, Quantifying mitochondrial content in living cells, in *Methods in cell biology*, Vol. 125 (Elsevier, 2015) pp. 77–93.
- [75] N. Zamponi, E. Zamponi, S. A. Cannas, O. V. Billoni, P. R. Helguera, and D. R. Chialvo, Mitochondrial network complexity emerges from fission/fusion dynamics, *Sci Rep* **8**, 1 (2018).
- [76] G. R. Lewis and W. F. Marshall, Mitochondrial networks through the lens of mathematics, *Physical biology* **20**, 051001 (2023).
- [77] C. Osman, T. R. Noriega, V. Okreglak, J. C. Fung, and P. Walter, Integrity of the yeast mitochondrial genome, but not its distribution and inheritance, relies on mitochondrial fission and fusion, *Proceedings of the National Academy of Sciences* **112**, E947 (2015).
- [78] C. Wang, W. Du, Q. P. Su, M. Zhu, P. Feng, Y. Li, Y. Zhou, N. Mi, Y. Zhu, D. Jiang, *et al.*, Dynamic tubulation of mitochondria drives mitochondrial network formation, *Cell research* **25**, 1108 (2015).
- [79] X. G. Arceo, E. F. Koslover, B. M. Zid, and A. I. Brown, Mitochondrial mrna localization is governed by translation kinetics and spatial transport, *Plos Comput Biol* **18**, e1010413 (2022).
- [80] C. Jakubke, R. Roussou, A. Maiser, C. Schug, F. Thoma, R. Bunk, D. Hörl, H. Leonhardt, P. Walter, T. Klecker, *et al.*, Cristae-dependent quality control of the mitochondrial genome, *Science advances* **7**, eabi8886 (2021).
- [81] K. Nakada, K. Inoue, T. Ono, K. Isobe, A. Ogura, Y.-I. Goto, I. Nonaka, and J.-I. Hayashi, Inter-mitochondrial complementation: mitochondria-specific system preventing mice from expression of disease phenotypes by mutant mtdna, *Nat Med* **7**, 934 (2001).
- [82] R. Bravo-Sagua, V. Parra, C. López-Crisosto, P. Díaz, A. F. Quest, and S. Lavandero, Calcium transport and signaling in mitochondria, *Comprehensive physiology* **7**, 623 (2017).
- [83] A. Raj, E. LoCastro, A. Kuceyeski, D. Tosun, N. Relkin, and M. Weiner, Network diffusion model of progression predicts longitudinal patterns of atrophy and metabolism in alzheimer’s disease, *Cell Rep* **10**, 359 (2015).
- [84] S. R. Dunbar, The average distance between points in geometric figures, *Coll Math J* **28**, 187 (1997).
- [85] O. Bénichou, C. Chevalier, J. Klafter, B. Meyer, and R. Voituriez, Geometry-controlled kinetics, *Nat Chem* **2**, 472 (2010).
- [86] D. J. Smith and M. K. Vamanamurthy, How small is a unit ball?, *Math Mag* **62**, 101 (1989).
- [87] A. E. Lefebvre, G. Sturm, T.-Y. Lin, E. Stoops, M. P. López, B. Kaufmann-Malaga, and K. Hake, Nellie: automated organelle segmentation, tracking and hierarchical feature extraction in 2d/3d live-cell microscopy, *Nature Methods* , 1 (2025).
- [88] S. Van der Walt, J. Schönberger, J. Nunez-Iglesias, F. Boulogne, J. D. Warner, N. Kaplan, D. Burt, M. Evans, T. Rossant, E. Marco, *et al.*, scikit-image: image processing in python, *PeerJ* **2**, e453 (2014).
- [89] J. Nunez-Iglesias, A. J. Blanch, O. Looker, M. W. Dixon, and L. Tilley, A new python library to analyse skeleton images confirms malaria parasite remodelling of the red blood cell membrane skeleton, *PeerJ* **6**, e4312 (2018).
- [90] E. F. Koslover and Z. C. Scott, *networktools* (2024).